THE JOURNAL OF PHYSICAL CHEMISTRY B
A JOURNAL OF THE AMERICAN CHEMICAL SOCIETY

pubs.acs.org/JPCB

Article

Photoelectron Spectroscopy of Benzene in the Liquid Phase and Dissolved in Liquid Ammonia

Published as part of The Journal of Physical Chemistry virtual special issue "Dor Ben-Amotz Festschrift".

H. Christian Schewe,* Krystof Brezina, Vojtech Kostal, Philip E. Mason, Tillmann Buttersack, Dominik M. Stemer, Robert Seidel, Wilson Quevedo, Florian Trinter, Bernd Winter, and Pavel Jungwirth*

Cite This: *J. Phys. Chem. B* 2022, 126, 229−238

Read Online

ACCESS | Metrics & More | Article Recommendations | Supporting Information

ABSTRACT: We report valence band photoelectron spectroscopy measurements of gas-phase and liquid-phase benzene as well as those of benzene dissolved in liquid ammonia, complemented by electronic structure calculations. The origins of the sizable gas-to-liquid-phase shifts in electron binding energies deduced from the benzene valence band spectral features are quantitatively characterized in terms of the Born−Haber solvation model. This model also allows to rationalize the observation of almost identical shifts in liquid ammonia and benzene despite the fact that the former solvent is polar while the latter is not. For neutral solutes like benzene, it is the electronic polarization response determined by the high frequency dielectric constant of the solvent, which is practically the same in the two liquids, that primarily determines the observed gas-to-liquid shifts.

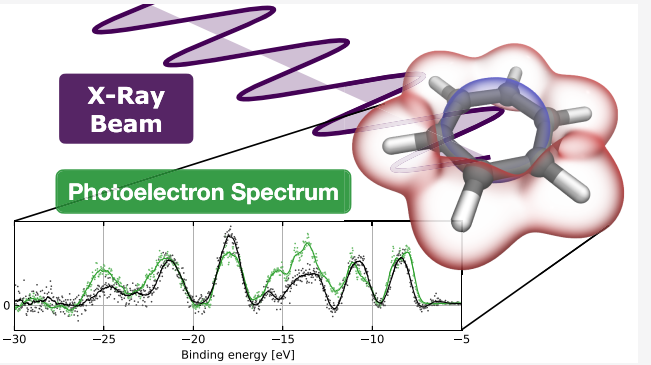

1. INTRODUCTION

The liquid microjet technique is a unique tool that enables measurement of the electronic structure of volatile solutions using X-ray photoelectron (PE) spectroscopy.[1−3] Being well established for water and aqueous solutions,[4] this approach has also been developed for cryogenic and room temperature nonpolar liquids[5,6] such as liquid nitrogen, liquid argon,[5] or most recently liquid ammonia and its solutions.[7,8] Using photoelectron spectroscopy (PES), we are now in a unique position to investigate solvent effects on the electronic structure of a solute molecule in a wide variety of nonpolar and polar liquids.

Benzene (C_6H_6) is the archetypal aromatic molecule. Its electronic structure has been thoroughly investigated in the gas phase using PES[9−12] as well as quantum chemical computational methods.[13−15] Despite theoretical studies,[16] PE spectra of neither pure liquid benzene nor benzene in solutions have been recorded so far with the closest study being a recent sophisticated PES measurement of gas and liquid trimethylbenzenes.[6] In the liquid state, the detailed vibrational structure of the PE spectra of gaseous benzene[12] is expected to be washed out similar to liquid water, while other interesting features may arise that include changes and shifts of the characteristic line shapes due to the presence of intermolecular interactions. As observed for other dissolved species, interactions with the local solvent environment lead to measurable shifts of the peaks in the PE spectra compared to their positions in the gas phase.[6,17] The size of these shifts depends on both the character of the solvent molecules and the charge of the solute.[1,18−20]

Here, we investigate the electronic structure of solvated benzene using PE spectroscopy and quantum chemical calculations. Experimentally, we exploit a recent development in liquid-microjet PES, which enables the measurement of accurate absolute electron binding energies (BEs).[19,21,22] Using this technique, we determine the BEs of pure liquid ammonia and benzene and also characterize the magnitude of solute-induced shifts on the solvent. In addition, we use quantum chemical calculations to guide the interpretation of the spectroscopic measurements. The principal result of the present study is that the shifts of the valence PE spectral features of benzene and ammonia from the gas to the liquid phase are sizable; however, the BE shift of benzene upon

Received: September 16, 2021
Revised: December 8, 2021
Published: December 22, 2021

https://doi.org/10.1021/acs.jpcb.1c08172
J. Phys. Chem. B 2022, 126, 229−238

solvation is almost the same in a liquid ammonia solution and in pure liquid benzene. This behavior can be rationalized by a simple thermodynamic cycle that approximates the solvent electronic polarization effects by the Born equation.

2. METHODOLOGY

2.1. Experimental Methods. *2.1.1. Experimental Details and Procedures.* Liquid ammonia solutions were prepared in an evacuated borosilicate glass cylinder (hereafter referred to as the condensation unit) embedded in a bath of cooled ethanol at −60 °C. After condensing a known volume of gaseous ammonia, (Westfalen, purity 5.0) defined amounts of NaI (Merck, purity 99.8%) were dissolved to generate 50 mM concentrations to ensure conductivity of the liquid ammonia solution in order to prevent streaming potentials.

In a subsequent step and depending on the experimental details, defined amounts of liquid benzene (Merck, purity 99.8%) were dissolved in a liquid ammonia solution as well. The solution was then transferred via a 6 mm diameter stainless steel tube from the condensation unit to the cryogenic unit (see Figure 1). The cryogenic unit itself consists of a

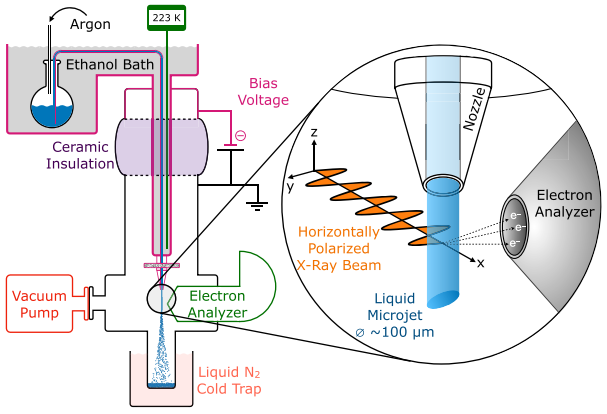

Figure 1. Experimental scheme illustrating how the cryogenic unit is mounted on top of the SOL^{3}PES. Details are given in the main text.

double-walled stainless steel container that is evacuated to ensure thermal insulation. An ∼50 mm diameter stainless steel tube mounted on top of the container feeds through a flange into the vacuum chamber. Liquid ethanol, cooled with liquid nitrogen, is recycled in the chamber using a commercial aquarium pump in order to keep the temperature of the ensemble constant at ∼220 K. Liquid nitrogen was frequently poured on top of the ethanol bath to cool it and to keep the temperature stable at ∼220 K.

The liquid microjet was generated by applying pressure of up to 5 bar of argon at the top of the sample cylinder. The ammonia solution was then pressed through the 6 mm diameter stainless steel tube and through a commercially available polyethylene filter at the end. The solution was released into vacuum through a quartz capillary (inner diameter of ∼100 μm), which was glued into the outlet of the filter. In contrast to the liquid ammonia experiments, studies with liquid benzene have been conducted at room temperature using the standard liquid jet setup described in ref 23. Here, an HPLC pump (Watrex) was used to push the liquid benzene through an ∼25 μm inner diameter nozzle into the vacuum chamber.

Two cooling traps and a 1500 L turbo-molecular pump maintained at least a pressure of $\sim 5 \times 10^{-4}$ mbar in the main vacuum chamber. All of the liquid jets formed a laminar flow for at least 2 mm before disintegrating into droplets while falling into the catcher unit. There, any residual liquid was frozen by placing a liquid nitrogen bath outside the vacuum chamber. Both microjet assemblies were mounted on top of linear $x-y-z$-manipulators onto which additionally a ceramic flange was mounted. This ensured electric insulation of the whole cryostat unit and the liquid jet itself relative to the main instrument; the insulated part is framed in red in the top left part of Figure 1. In turn, this allowed the application of a DC bias voltage U using a power supply (Delta Elektronika). The polarity was chosen such that the main chamber and especially the electron analyzer were grounded, while the cryostat unit and, thus, the liquid jet had negative polarity. The resulting electric field accelerated the photoelectrons toward the electron analyzer. The right inset of Figure 1 depicts in a schematic way the interaction of the microjet flowing down vertically from the top where it is illuminated by the synchrotron beam propagating along the x-direction, while the photons linear polarization axis lies in the $x-y$-plane. Photoelectrons were collected parallel to the polarized electric field vector with the electron analyzer lying in the $x-y$-plane.

PE measurements were carried out on the SOL^{3}PES setup[23] at the U49/2-PGM-1 beamline[24] at the BESSY II electron storage ring operated by the Helmholtz-Zentrum Berlin für Materialien und Energie. Valence PE spectra were recorded using a photon energy of $h\nu = 123.464 \pm 0.004$ eV, which was calibrated on a daily basis by measuring the photoelectron yield. We specifically obtained the so-called electron-yield X-ray absorption spectra generated by the integration of the electron emission arising from the 2p3p3s Auger decay channel of an argon resonance at $h\nu = 246.928$ eV.[25] Note that at $h\nu = 123.464$ eV a 10% contribution from the respective second harmonic light ($h\nu = 246.928$ eV) is present. The instrumental energy resolution for all measurements is ∼30 meV (fwhm) determined by the settings of the electron analyzer (25 meV) and the beamline (16 meV). The X-ray spot size was defined by the beamline exit slit and had a rectangular shape of 40 × 60 μm^2 (horizontal × vertical).

2.1.2. Absolute Binding Energies. Upon application of a negative bias voltage U onto the electrically insulated microjet, the photoelectrons from the liquid are accelerated toward the grounded electron analyzer. As commonly done, we dissolved small amounts of ionic charge carriers (typically ∼50 mM) of, e.g., NaI or tetrabutylammonium iodide (TBAI) to ensure the conductivity of the solutions. This enables one to bias the whole liquid with the applied offset potential U[21,22] and to discharge local streaming potentials or the positive charging caused by the photoionization process.[21,22,26] Thus, the kinetic energies (KEs) of the whole liquid-phase PE spectrum are shifted by the energy-offset eU, where e is the elementary charge. This allows one to measure the kinetic energy (KE_{SF}) corresponding to a particular spectral feature[19,21,22] and, at the same time, to detect the electron distribution of the low kinetic energy curve, resulting mostly from inelastically scattered electron processes.[27,28] Most importantly, the onset of the low kinetic energy distribution defines the smallest electron KE by which a photoelectron can just be ionized and can escape the solution into vacuum, denoted here as KE_{cut}. Hence, we determine KE_{cut} by fitting the onset of the low kinetic energy distribution; the details are discussed in ref 21 and the

https://doi.org/10.1021/acs.jpcb.1c08172
J. Phys. Chem. B 2022, 126, 229−238

Supporting Information. Thus, the energy difference of $KE_{SF} - KE_{cut}$ at a given $h\nu$ allows one to determine the absolute binding energy of a particular spectral feature BE_{SF} with respect to the vacuum ionization potential as

$$BE_{SF} = h\nu - (KE_{SF} - KE_{cut}) \quad (1)$$

This procedure is hereafter referred to as "absolute BE determination". This BE calibration method is accurate, unlike calibration methods where gas-phase peaks are related to liquid-phase ones, because any kind of offset or contact potential induces an equal and simultaneous shift of the spectral features (KE_{SF}) and the KE_{cut}. Typical sources for these offset potentials are the streaming potential or the charging induced by the photoionization.[21] As long as the offset potentials remain constant as a function of time, also the value of the applied bias voltage U can be conveniently chosen. Figure 3 shows an example of this method: the left and right parts of the upper panel, respectively, show the low kinetic energy curve and the valence band (VB) PE features of a 50 mM NaI liquid ammonia solution as a function of the measured KE illustrated by the top horizontal axis. Note that the steep slope of the low kinetic energy curve is located at KE ~ 50 eV, resulting from the applied bias voltage of $U = -50$ V. The BE axis illustrated at the bottom horizontal axis has been determined using the calibrated photon energy of $h\nu = 123.464 \pm 0.004$ eV.

2.1.3. Gas-to-Liquid-Phase Binding Energy Shifts. In order to obtain a physically motivated estimate of the gas-to-liquid BE shifts of solutes, including benzene in liquid ammonia as well as in pure liquid benzene, we use the relevant Born–Haber thermodynamic cycle[29] in combination with the Born equation for solvation free energies in a dielectric continuum. This cycle is illustrated in Figure 2.

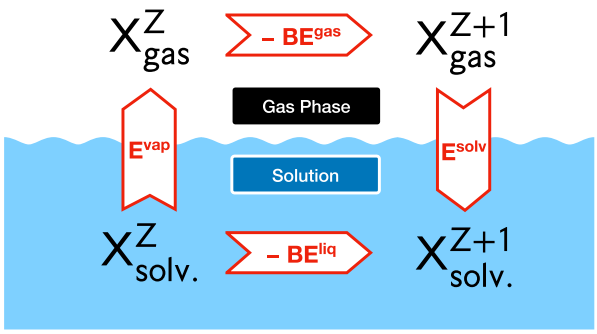

Figure 2. Schematic illustration of the Born–Haber cycle: when probing the neutral solute ($Z = 0$) of, e.g., X being benzene via photoionization in a given solvent, the solute changes its oxidation number and becomes in the present case the benzene radical cation ($Z + 1 = 1$).

By summing the cycle up, we find that the gas-to-liquid BE shift $\Delta^{BH}BE$ can be expressed as

$$\Delta^{BH}BE = BE^{liq} - BE^{gas} = -(E^{vap} + E^{solv}) \quad (2)$$

where BE^{liq} is the vertical BE in the liquid environment, BE^{gas} is the vertical BE in the gas phase, E^{vap} is the vaporization free energy and, finally, E^{solv} represents the solvation free energy.

Clearly, the respective values of the vaporization and solvation free energies of oxidation states of species X prior to (X^{Z}_{solv}) and after (X^{Z+1}_{solv}) the photoionization have to be known in order to apply the Born–Haber cycle in Figure 2. Within the dielectric continuum description of the solvent, these quantities, generally denoted as changes in Gibbs free energy, ΔG, are approximated by the well-known Born equation[30]

$$\Delta G = \frac{Z^2 e^2}{8\pi\epsilon_0 R}\left(1 - \frac{1}{\epsilon_r}\right) \quad (3)$$

where Z is the oxidation number of the solute, ϵ_0 is the vacuum permittivity, ϵ_r is the relative dielectric constant of the environment, and R is the effective radius of the sphere that approximates the shape of the solute. In contrast to the fully relaxed solvation processes described by the Born equation, PES probes vertical BEs of the final ionized state X^{Z+1}_{solv}, which corresponds to the ionization processes happening on much faster time scales than needed for solvent reorganization. Therefore, the photoionization of the initial state X^{Z}_{solv} induces only electronic relaxation of the solvent without a rearrangement of the molecular geometry.[29]

In order to be able to close the Born–Haber cycle, the solvation free energy, E^{solv}, must thus describe only the electronic part of the solvent relaxation during solute solvation. This is accounted for by replacing the full static dielectric constant, ϵ_r, by its high frequency limit, which is equal to the square of the refractive index, n^2. This yields the relevant modified form of the Born equation for E^{solv}

$$E^{solv} = \frac{Z^2 e^2}{8\pi\epsilon_0 R}\left(1 - \frac{1}{n^2}\right) \quad (4)$$

Importantly, the corresponding vaporization free energy, E^{vap}, is zero for neutral species with $Z = 0$ within the continuum electrostatic description as follows from eq 3. For realistic systems, the (nonzero) vaporization enthalpy and entropy data are tabulated for common compounds[31] and the corresponding free energies are calculated in the Supporting Information. However, even in realistic systems, this quantity can be neglected in comparison to the solvation energy, E^{solv}, of the nascent radical cations (Figure 2) since it is typically on the order of the error bar (as shown below). It follows that the gas-to-liquid shift depends only on the value of E^{solv} and, consequently, only on the refractive index, n, of the surrounding solvent. Since its typical values lie in the range from 1.3 to 2.0 for most solvents, in spite of the fact the corresponding static dielectric constants may vary by an order of magnitude, the Born–Haber model predicts that gas-to-liquid shifts will be similar for neutral solutes among a multitude of solvents. Note that, if the initial state ($X^{Z\neq 0}_{solv}$) was charged, the situation would be quite different as one could not exclude the solvent nuclear reorganization and the corresponding dependence on ϵ_r from the picture. The effect of the specific choice of solvent on gas-to-liquid shifts of charged solutes is discussed in refs 1 and 20.

Last to discuss is the estimation of the solute effective radius, R, to be used in eq 4. In this work, we use the first maximum of the relevant radial distribution function (RDF), while the deviation of the molecular structure from a perfect sphere is estimated using the width of the corresponding RDF peak. Note that, the more the molecular geometries deviate from the

https://doi.org/10.1021/acs.jpcb.1c08172
J. Phys. Chem. B 2022, 126, 229–238

assumed spherical shape, the less accurate the Born equation and the following gas-to-liquid BE shift estimates become.

2.2. Computational Methods. *2.2.1. Gas-Phase Calculations.* The gas-phase thermal structures of benzene were sampled using ab initio molecular dynamics (AIMD) performed in CP2K 7.1 software equipped with the Quickstep module.[32] The energies and forces were obtained on the fly using the revPBE0-D3[33−36] hybrid density functional to describe the valence electronic structure, while the carbon core electrons were modeled by the Gödecker-Tetter-Hütter (GTH) pseudopotentials.[37] The Kohn−Sham orbitals were expanded into the TZV2P-MOLOPT-GTH primary basis set,[38] and the electron density was represented in a plane wave basis capped at the energy of 600 Ry. To accelerate the calculation, we additionally employed the Auxiliary density matrix method with the cpFIT3 fitting basis set.[39] To comply with the employed Poisson electrostatics solver, the simulated molecule was placed into a 11 Å wide cubic box and kept in its center throughout the course of the simulation; however, the boundary conditions were kept open. With these settings, the nuclei were numerically propagated using the Verlet integrator with a 0.5 fs integration time step. Canonical sampling was ensured by a local stochastic velocity thermostat[40] with a 50 fs time constant keeping the temperature fixed at 300 K, and the total simulated time was 20 ps. The G_0W_0 calculations[41,42] were performed consistently in the CP2K 7.1 software package on top of the AIMD geometries separated by 20 fs. The same DFT method and primary basis were employed to calculate the initial Kohn−Sham wave function, and the RI-TZ resolution-of-identity auxiliary basis set was used to decompose the Hartree−Fock integrals. The self-energy was continued analytically on the real frequency axis using the Padé approximation, and the Newton−Raphson fixed point iteration was used for the numerical solutions.

2.2.2. Calculations in Liquid Ammonia. The solution of benzene in liquid ammonia was simulated with a similar computational methodology to the one described above for the gas phase. The liquid ammonia environment surrounding the benzene molecule was represented using 64 explicit solvent molecules under periodic boundary conditions; this corresponds to a simulated concentration of 0.65 mol l^{-1}. In this case, the temperature was set to 223 K to keep the solvent liquid and the total simulated time was 100 ps. The G_0W_0 calculations were consistently performed on top of the simulated ensemble of explicitly solvated structures. A detailed description of the performed condensed-phase simulations can be found in refs 16 and 43.

3. RESULTS AND DISCUSSION

3.1. Gas−Liquid-Phase Shift in Ammonia. The upper panel of Figure 3 shows in its left and right part the measured PE spectrum of the low kinetic energy curve and the VB, respectively, as a function of the kinetic energy (on the top horizontal axis) with the binding energy axis (plotted as the horizontal axis at the bottom) being absolute BE determined using eq 1. The liquid highest occupied molecular orbital (HOMO) corresponding to the $3a_1$ molecular orbital of the gas phase ammonia molecule is determined at $BE_{3a_1}^{liq} = -8.96 \pm 0.02$ eV. This value is in good agreement with the value of $BE_{3a_1}^{liq} = -9.09 \pm 0.05$ eV stated in ref 17. There, the binding energy calibration was performed by referencing the gas-phase peak to a previously determined value of $BE_{3a_1}^{gas}$ = −10.93 eV.[44] Using $BE_{3a_1}^{gas}$, we now determine the gas-to-liquid shift in ammonia to be $\Delta BE_{NH_3} = -1.97$ eV, which differs only by 13 meV compared to the value stated in ref 17; small systematic errors may have led to the cancellation of errors in the assignment done in the previous paper as pointed out in the Supporting Information.

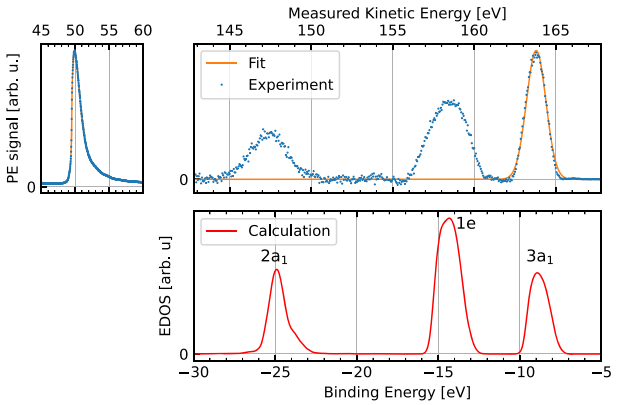

Figure 3. Top left and right parts depict the low kinetic energy curve and the valence band PE spectrum (blue dotted line) of a 50 mM NaI liquid NH_3 solution, both shifted by ∼50 eV upon application of a bias voltage of $U = -50$ V. The indicated fits (red curves) to the low kinetic energy curve and the liquid HOMO ($3a_1$) enable one to determine the liquid-phase binding energy axis, depicted in the lower panel, on an absolute scale using the well calibrated photon energy of $h\nu = 123.464 \pm 0.004$ eV. Bottom: the comparison with the calculated electronic density of states (red line) using the G_0W_0 method clearly shows that the experimental spectral features are broadened.

The experimental liquid ammonia spectrum is in excellent agreement with the theoretical prediction of the electronic density of states[17] (EDOS) calculated by a combination of condensed-phase AIMD and G_0W_0 calculations[41] performed on the obtained thermal structures, which are shown as the red curve in the lower panel of Figure 3. Note that, while the relative peak positions between the experiment and the calculation are reproduced extremely well, the predicted peak widths are systematically smaller in the theoretical data. This effect is common to all calculations of this type and is caused by a combination of several factors. Notably, the calculation relies on classical AIMD and, therefore, samples, unlike the experiment, a classical ensemble of the configurations. Moreover, the experiment captures inelastic scattering processes, which lead to slightly asymmetric line shapes toward higher BEs in the experimental spectra; the description of this goes beyond the level of theory used here.

We calculated the gas-to-liquid shift of ammonia in liquid ammonia to be $\Delta^{BH}BE_{NH_3}^{NH_3(l)} = -2.01$ eV using eq 4. For this, we estimate the radius R using half of the distance estimated for the maximum of the first peak of the RDF in ammonia. The average nitrogen−nitrogen distance is 3.45 Å.[45] These estimates from the Born−Haber approximation thus recover the measured gas-to-liquid shift in ammonia of $\Delta BE_{NH_3} = -1.97$ eV extremely well.

There are a number of other effects that are not captured within the Born model such as the dipole−dipole interactions between the ammonia molecules or various effects at the liquid surface. There is a contribution to the gas-to-liquid shift from a net surface dipole resulting from the orientation of dipolar

https://doi.org/10.1021/acs.jpcb.1c08172
J. Phys. Chem. B 2022, 126, 229−238

molecules at the surface. For example, this has been calculated to be ∼0.14 eV for water.[46,47] Since we can only speculate about the orientation of ammonia at the liquid surface, we assume the value of the surface potential to be smaller for ammonia. The surface dipole effect of benzene should be zero, since benzene does not possess a permanent electric dipole moment. Other sources for potential differences can result from surface active species in contrast to bulk active species.[48] In conclusion, all these effects only have minor influences on the gas-to-liquid phase BE shift in terms of their order of magnitude compared to the major contribution conceived within the Born−Haber model.

3.2. Gas-Phase Benzene. The top panel of Figure 4 depicts the gas-phase PE spectrum of benzene, which has been

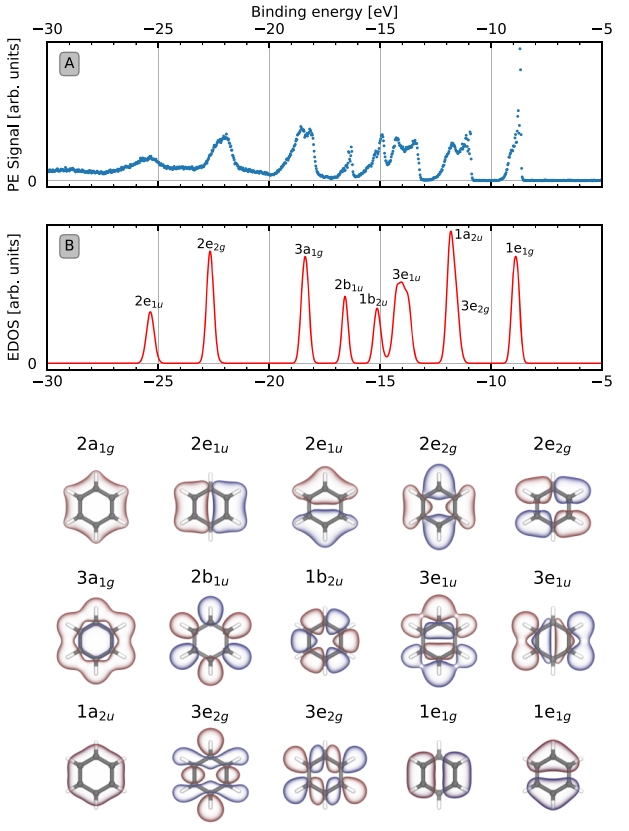

Figure 4. Electron binding energies of gas-phase benzene. (A) PES spectrum of the gas phase. (B) Calculated electronic density of states using the G_0W_0 method. Bottom: Kohn−Sham canonical molecular orbitals of minimum-geometry benzene calculated by the revPBE0-D3/TZV2P-MOLOPT-GTH method. The red surface shows a contour of the orbitals at 0.025 $a_0^{-3/2}$ and the blue surface, a contour at the same magnitude with a negative sign.

recorded by moving the liquid jet out of the synchrotron light beam such that only benzene molecules that evaporated from the liquid surface are ionized. The binding energy of the spectrum has been calibrated like the spectrum shown in the top panel of Figure 5; details are discussed in the section on Liquid Benzene.

Following ref 12, the spectral features as a function of decreasing binding energy can be assigned to the molecular orbitals $1e_{1g}$, $3e_{2g}$, $1a_{2u}$, $3e_{1u}$, $1b_{2u}$, $2b_{1u}$, $3a_{1g}$, $2e_{2g}$, $2e_{1u}$, and $2a_{1g}$, which represent the electronic configuration of the neutral

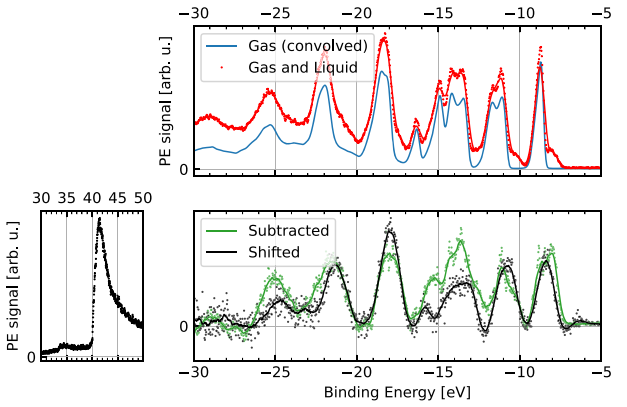

Figure 5. Top panel: measured gas-and-liquid-phase spectrum (red line) and gas-phase spectrum (blue line) from a pure liquid benzene microjet (without any salt). Bottom panel: liquid-phase PE spectrum of benzene derived via the two different procedures as described in the main text: the difference spectrum resulting from the subtraction of the spectra in the upper panel is plotted in green. The spectra of the low kinetic energy curve and the VB of the 50 mM TBAI solution mixture, consisting of 90% benzene and 10% 2-propanol, are shown in black in the left and right panel, respectively. Note: the low kinetic energy curve is plotted as a function of the measured kinetic energy upon the application of a bias of −40 V, while the VB has been the absolute BE determined and plotted as a function of BE to give a better comparison to the difference spectrum shown in green.

single-determinant ground state. The orbitals $1e_{1g}$, $3e_{2g}$, and $3a_{1g}$ show a vibrational progression very similar to the spectra shown in ref 12, which contains the most recent benzene gas-phase investigation containing the best resolved spectra.

The binding energy of the gas-phase HOMO $1e_{1g}$ has been determined from the peak maximum of the convoluted experimental data as $BE_{1e_{1g}}^{gas,exp} = -8.92 \pm 0.08$ eV, which is in excellent agreement with the mean of the calculated HOMO of $BE_{1e_{1g}}^{gas,calc} = -8.90$ eV, as shown in the lower panel of Figure 4.

Consistent with the previously published theoretical data focusing on liquid ammonia[17] (Figure 3, bottom panel), the gas-phase benzene experimental peak positions are closely reproduced by the G_0W_0 calculations. The individual peaks in the calculated EDOS were furnished with the corresponding orbital irreducible representation labels, and the assignment was confirmed by comparison of the calculated degeneracies with those predicted by the symmetry labels (see Section S7) as well as by the comparison of the labels with the symmetries of the spatial orbitals themselves. These are shown in the bottom part of Figure 4. However, it appears that the calculation at the chosen level of theory systematically tends to underestimate energy differences between close-to-degenerate levels (in particular the $1a_{2u}$ and $3e_{2g}$ peaks) and, as a result, the resolution in several experimental peaks is suppressed in the computational counterpart. In Section S6, we discuss that the simple iterative version of G_0W_0, the evGW method,[42] allows one to recover some of these missing features but also causes an overall worsening of the EDOS quality. Moreover, note that the gas-phase experiment captures the fine vibrational structure clearly in several peaks; this effect is not reproduced by the calculations that build on classical thermal structures with a continuous energy distribution. In this direction, far more advanced calculation methods are available for gas-phase systems;[12] however, the present computational

https://doi.org/10.1021/acs.jpcb.1c08172
J. Phys. Chem. B 2022, 126, 229−238

results are sufficient for the investigations we undertake here, since we are primarily interested in the BE shift of the gas-to-liquid-phase peak upon solvation. These gas-phase calculations are methodologically complementary to the ones used for the liquid system and, therefore, represent a reasonably consistent foundation to compare the theoretical results to the experimentally determined ones. In general, our findings are in good agreement with the values stated in ref 12, where the gas-phase HOMO is experimentally determined to be −9.24 eV and computationally to be −9.12 eV without additional error bars.

3.3. Liquid Benzene. The liquid phase VB spectrum of benzene has been measured using two different procedures in the experiment with details of the analysis given in the Supporting Information. Only the two procedures combined allowed one to unambiguously determine the valence band peak structure and its absolute calibrated BEs. This is a consequence of the fact that we have not managed to dissolve considerable amounts of ionic species in pure liquid benzene to ensure sufficient conductivity; therefore, we needed to admix a small amount of a second solvent in addition to the salt. First, the gas-and-liquid-phase spectrum of pure liquid benzene (without any salts dissolved) has been measured and is plotted as a red line in the upper part of Figure 5. It is shown together with the pure gas-phase spectrum (blue line). The respective liquid-only PE spectrum is obtained from the difference between the two spectra, which is plotted as green dots in the lower part of Figure 5 (the green line corresponds to a convolution of the experimental data by a box kernel 20 data points wide). The pure gas-phase spectrum (blue line) has been convoluted using a Gaussian function with a full-width-at-half-maximum of 0.11 eV to match the broadened gas-phase peaks of the gas-and-liquid-phase spectrum in order to avoid artificial peaks in the subtraction process.

In our second approach, we used a 50 mM TBAI solution mixture consisting of 90% benzene and 10% 2-propanol. In this way, we could dissolve ions in a sufficient amount in the benzene and 2-propanol mixture to ensure conductivity, which was impossible in pure benzene. This allowed us to apply a bias voltage on the liquid jet to enable the same procedure as for ammonia to determine absolute BEs of the liquid-phase spectral features by additionally determining KE_{cut}. The left part of the lower panel of Figure 5 depicts the spectrum of the low kinetic energy curve as a function of the kinetic energy, while the right part shows the VB spectrum as a function of the binding energy (absolute BE determined). The black straight line again corresponds to a convolution of the data points with a box kernel as above. Qualitatively, the two different experimental procedures yield almost the same BEs of the individual spectral features of the VB of the liquid phase of benzene, which can clearly be distinguished. The solid green and black lines indicate intensity fluctuations of the same peak. A comparison of the scatter plots of the individual data points shows that the spectral features also coincide quantitatively well within the experimental uncertainty. We find that the liquid phase spectrum can essentially be considered as a shifted and slightly broadened gas-phase spectrum and the same gas-phase orbital assignment can directly be applied.

Using the analysis described in the Supporting Information, the absolute BE determination procedure has been performed using the photon energy of $h\nu$ = 123.464 eV. The BE of the liquid-phase HOMO corresponding to the gas-phase $1e_{1g}$ orbital ($BE^{liq}_{1e_{1g}}$) has been determined in the experiment to be −8.42 ± 0.05 eV. Using the absolute BE method together with the known benzene gas-phase energy ($BE^{gas}_{1e_{1g}}$) of −9.24 eV,[12] we determine the gas-to-liquid-energy shift to be $\Delta BE^{C_6H_6(l)}_{C_6H_6}$ = −0.82 ± 0.05 eV. This value is only slightly larger than the $\Delta BE^{C_6H_6(l)}_{C_6H_6}$ value of 0.50 ± 0.18 eV obtained when we apply the gas-phase reference method using the spectra of gas-phase and gas-and-liquid-phase benzene shown in Figure 5. Comparing this to the estimate of the Gibbs free energy of solvation using the Born equation where we approximated $\Delta^{BH}BE^{C_6H_6(l)}_{C_6H_6}$ = −1.36 eV using R = 2.95 Å,[49] we find that the Born−Haber model overestimates the gas-to-liquid shift compared to the experimentally determined one of $\Delta BE^{C_6H_6(l)}_{C_6H_6}$ = −0.82 ± 0.05 eV by ∼0.5 eV. We attribute this discrepancy to the fact that the benzene molecular geometry is planar and thus deviates to a large extent from a sphere, which is assumed in the derivation of the Born equation.

3.4. Benzene in Liquid Ammonia. The top panel of Figure 6 shows the measured VB PE spectrum of a solution of a 0.05 M NaI + 0.25 M benzene in liquid ammonia (blue data points). The binding energy axis has been the absolute BE determined using a bias voltage of U = −50 V, together with a calibrated photon energy of $h\nu$ = 123.464 eV. The computational prediction of the EDOS (red curve) well reproduces not only the overall VB spectral shape but also the individual BE peak positions. All experimentally recorded spectral features

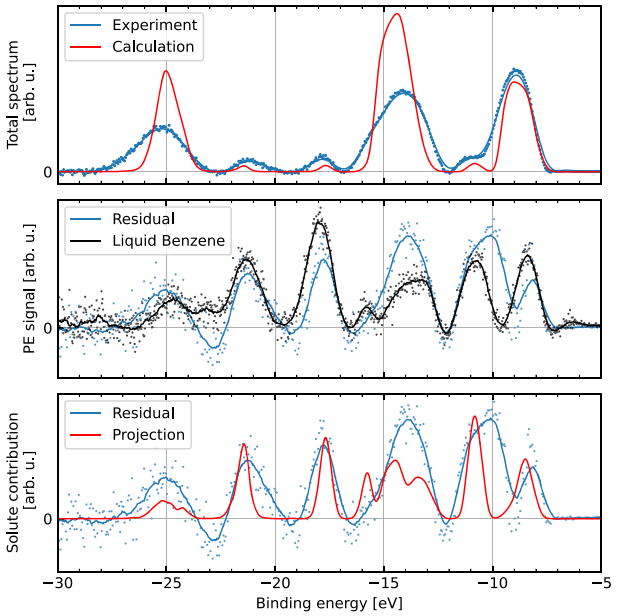

Figure 6. Experimental results and theoretical prediction of the XPS of the liquid ammonia solution of benzene. Top panel: The total PE spectrum of 0.05 M NaI and 0.25 M benzene in liquid ammonia (blue data points) and the computational prediction of the EDOS corresponding model (red curve). Central panel: Difference spectrum (residuals, blue curve) of the 0.05 M NaI and 0.25 M benzene in liquid ammonia spectrum minus the pure ammonia spectrum shown in the top panel of Figure 3 is plotted together with the benzene and 2-propanol spectra (black curve); both spectra are absolute BE determined values. Bottom panel: The same difference spectrum (residuals, blue curve) corresponding to the solute contribution is compared to the theoretical benzene PDOS.

https://doi.org/10.1021/acs.jpcb.1c08172
J. Phys. Chem. B 2022, 126, 229−238

show a peak broadening relative to the computed ones, as discussed previously.

The central panel of Figure 6 shows a difference spectrum (residuals) where the pure ammonia spectrum shown in the top panel of Figure 3 has been subtracted from the experimentally recorded 0.05 M NaI + 0.25 M benzene in the liquid ammonia spectral intensity distribution shown in the top panel of Figure 6. It has been calculated by first scaling the peak maximum of the liquid HOMO of each spectrum to unity, while the BE axis in both spectra is the absolute BE determined value before the subtraction has been performed. The residual spectral intensity is plotted as blue dots in the central and bottom panel of Figure 6 together with the experimentally determined liquid phase VB spectrum of the benzene and 2-propanol solution (black curve), which is also shown in Figure 5. The VB peaks of both spectra coincide very well, comparing the centroid BE positions as well as their spectral shapes. The only part of the VB where discrepancies appear in the residuals relative to the pure benzene spectrum are between the peaks corresponding to the molecular orbitals of $1e_{1g}$ and $3e_{2g}$. The liquid HOMO peak seems compressed at higher binding energies, while the $3e_{2g}$ peak seems broadened at lower BEs: we attribute this discrepancy to be an artifact resulting from the subtraction procedure.

The agreement between the two independently constructed spectra provides strong experimental evidence that a solution of solvated benzene in ammonia may be understood as a simple sum of its constituent parts (i.e., the pure liquid-phase spectra of benzene and ammonia). The bottom panel of Figure 6 depicts again the experimental residuals resulting from the subtraction and the calculated projected density of states (PDOS) of benzene in liquid ammonia, which has been projected onto the appropriate atomic basis functions localized on benzene and thus shows only the solute contribution.[16,50]

Using eq 4, the solvation free energy of the benzene radical cation in liquid ammonia has been calculated as $\Delta^{BH}BE_{C_6H_6}^{NH_3(l)} = -1.18$ eV; we use the same radius (R) of 2.95 Å[49] as in the case of benzene in liquid benzene, and the details are given in the Supporting Information. Similar to the case of benzene in liquid benzene, we attribute the discrepancy between $\Delta BE_{C_6H_6}^{NH_3(l)} = -0.82$ eV and $\Delta^{BH}BE_{C_6H_6}^{NH_3(l)} = -1.18$ eV to the large deviation of the planar molecular geometry of benzene relative to a sphere. However, when comparing the values of $\Delta^{BH}BE_{C_6H_6}^{NH_3(l)} = -1.18$ eV and $\Delta^{BH}BE_{C_6H_6}^{C_6H_6(l)} = -1.36$ eV, they only differ by 0.18 eV. Despite the fact that the approximated absolute values differ from the experimental ones by ∼0.5 eV, the modified Born model given in eq 4 estimates almost the same solvation free energy. The replacement of the static dielectric polarizability by the fast component of the dielectric response essentially captures the observed phenomenon: while we have observed large BE shifts of the VB peaks for benzene and ammonia upon solvation from the gas phase, the solvation of benzene in ammonia induces practically no measurable BE shifts compared to the situation in pure liquid benzene.

3.5. Surface Activity of Benzene in Liquid Ammonia. Upon using a photon energy of ∼123 eV, we are probing approximately 1−3 nm into the liquid phase.[4] This corresponds on average to 3−10 monolayers when assuming the average interparticle distance of ammonia to be ∼0.345 nm (details are given in the Supporting Information). As shown in the previous section, the spectra of benzene dissolved in liquid ammonia can be decomposed using a simple addition of the pure benzene and pure ammonia spectra; therefore, we do not anticipate BE shifts of individual spectral features when going from the bulk to the surface. At the same time, benzene is expected to be surface active in liquid ammonia, which should result in an observable effect when comparing the ratio of the integrated spectral intensity of benzene relative to that of ammonia.

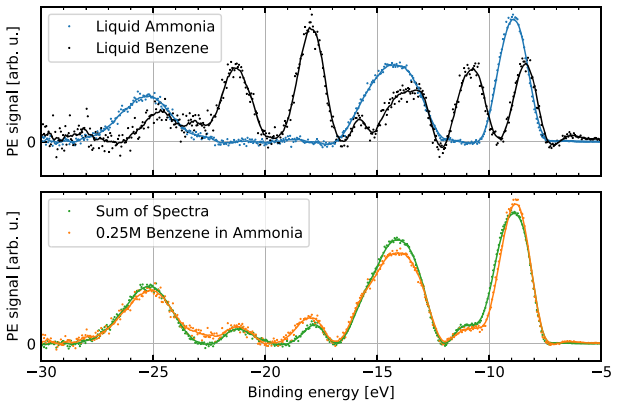

Figure 7. Top panel: normalized VB PE signal intensities of pure benzene ($I_{C_6H_6}$, black curve) and of ammonia (I_{NH_3}, blue curve) plotted as a function of the BE using the absolute BE determination. Lower panel: a weighted sum of both normalized pure spectra (green line).

The top panel of Figure 7 shows the normalized VB PE signal intensities of pure liquid benzene ($I_{C_6H_6}$, black curve) and of pure liquid ammonia (I_{NH_3}, blue curve) plotted as a function of the BE using the absolute BE determination. For the normalization process, the areas under all spectral features of the entire VB have been summed up such that all VB ionization features are captured. The lower panel of Figure 7 shows a weighted sum of both normalized pure spectra (green line) where $I_{C_6H_6}$ has been scaled by a factor α before it was added to I_{NH_3}. An optimizing procedure has been implemented where the factor α is manipulated until the area of the weighted sum spectrum equals the area of the measured spectrum of 0.25 M benzene in liquid ammonia (yellow line in Figure 7 and further details on the procedure in the Supporting Information). The sum spectrum (green line) corresponds well with the measured spectrum of 0.25 M benzene in liquid ammonia (yellow line), which gives us confidence in our conclusions of the additivity of the spectra of the individual species.

Thus, the ratio of spectral intensities $I_{C_6H_6}/I_{NH_3} = 0.2$ has been determined, meaning that the normalized spectral intensity of benzene observed in the PE studies is ∼5 times smaller than the one of ammonia.

At the same time, in the solution prepared for the experiment, the concentration was 0.25 mol l^{-1}. By taking the number of valence electrons and the atomic abundances of the two different molecules into account, we get a ratio that reflects the density of populated states (DoS) of the VB: $DoS_{C_6H_6}/DoS_{NH_3} \sim 1/44$. This ratio reproduces quantitatively the ratio of ∼1/43 of the EDOS determined from the

https://doi.org/10.1021/acs.jpcb.1c08172
J. Phys. Chem. B 2022, 126, 229−238

theoretical calculations (red curve shown in the top panel of Figure 6).

In order to compare the ratio of the DoSs with the ratio of the signal intensities of the measured spectrum, properties of the ionization process during the photoemission process need to be accounted for, namely, the different ionization cross sections as well as the anisotropies related to the experimental geometries (details of this calculation are given in the Supporting Information). Thus, the ammonia peak areas should be about ∼147 times larger than the benzene ones. The discrepancy between the ratio of ∼5 observed in the measured PE spectra and the above deduced ratio of ∼147 can be explained by assuming that benzene is surface active. Following this reasoning, we can deduce that the concentration of benzene at the surface is on average about an order of magnitude higher than in the bulk. This implies the possibility of aggregation alongside an increased benzene−benzene interaction or even phase separation of the solute on the liquid microjet surface, which would provide an alternative explanation of the observed spectral additivity. There is no practical way to judge the state of the jet surface experimentally with the current setup in order to completely exclude the possibility of a phase separation. However, there are several arguments favoring that our results are not a product of phase segregation. When estimating an error of the above approximation (details are given in the Supporting Information), we conclude that the uncertainty by which the concentration of benzene is enriched at the surface is >20%. The liquid jet is in a nonequilibrated state when it is released into vacuum; there is significant evaporation going on from its surface into the vacuum, which in turn, induces the rearrangement of the particles at the surface. Additionally, by comparison with the theoretical calculations of the benzene−ammonia solution where the solute is fully solvated at all times and where the spectral additivity is preserved, we conclude that the experimentally observed additivity must be possible without phase separation and corresponds simply to what is anticipated for a surface-active species like benzene in liquid ammonia.

4. CONCLUSION

The major finding of this combined experimental and computational study is the observation of large solvent-induced shifts in valence electron binding energies of benzene, as observed via X-ray PE spectroscopy. Notably, these gas-to-liquid shifts are almost the same for liquid ammonia as a polar solvent and pure benzene as a nonpolar one. This observation can be rationalized in terms of the Born−Haber solvation model. When interpreting shifts in electron binding energies extracted from the PE spectra, this model accounts for the solvent response to charged solutes only. In the case of solutes that are neutral before photoionization, such as benzene in the present case, the solvent shift within the Born−Haber model is solely due to the high frequency dielectric response of the solvent to the nascent benzene radical cation. The vertical photoionization process does not involve any nuclear solvent relaxation around the newly formed cationic solute. This explains why the solvent-induced shifts are practically the same in liquid ammonia and in benzene; while these two liquids have very different static dielectric constants (reflecting different nuclear relaxation in polar vs nonpolar solvents), their high frequency dielectric constants (due to electronic relaxation) are almost the same.[51]

■ ASSOCIATED CONTENT

Supporting Information

The Supporting Information is available free of charge at https://pubs.acs.org/doi/10.1021/acs.jpcb.1c08172.

Experimental measurement of the solubility of benzene in ammonia; calibration procedure of the absolute binding energies; detailed discussion of the estimation of the solvation energy using the Born equation; spectral intensity estimation for the benzene−ammonia solution; gas-to-liquid shift in pure ammonia; comparison of G_0W_0 and evGW calculation for gas-phase benzene; gas-phase benzene orbital assignment (PDF)

■ AUTHOR INFORMATION

Corresponding Authors

H. Christian Schewe − *Institute of Organic Chemistry and Biochemistry of the Czech Academy of Sciences, 166 10 Prague 6, Czech Republic*; Email: hanns_christian.schewe@uochb.cas.cz

Pavel Jungwirth − *Institute of Organic Chemistry and Biochemistry of the Czech Academy of Sciences, 166 10 Prague 6, Czech Republic*; orcid.org/0000-0002-6892-3288; Email: pavel.jungwirth@uochb.cas.cz

Authors

Krystof Brezina − *Charles University, Faculty of Mathematics and Physics, 121 16 Prague 2, Czech Republic; Institute of Organic Chemistry and Biochemistry of the Czech Academy of Sciences, 166 10 Prague 6, Czech Republic*; orcid.org/0000-0003-0285-1282

Vojtech Kostal − *Institute of Organic Chemistry and Biochemistry of the Czech Academy of Sciences, 166 10 Prague 6, Czech Republic*; orcid.org/0000-0001-6056-0817

Philip E. Mason − *Institute of Organic Chemistry and Biochemistry of the Czech Academy of Sciences, 166 10 Prague 6, Czech Republic*; orcid.org/0000-0002-3263-2825

Tillmann Buttersack − *Molecular Physics, Fritz-Haber-Institut der Max-Planck-Gesellschaft, D-14195 Berlin, Germany*; orcid.org/0000-0002-4547-2656

Dominik M. Stemer − *Molecular Physics, Fritz-Haber-Institut der Max-Planck-Gesellschaft, D-14195 Berlin, Germany*; orcid.org/0000-0002-5528-1773

Robert Seidel − *Helmholtz-Zentrum Berlin für Materialien und Energie, D-14109 Berlin, Germany*; orcid.org/0000-0003-2613-4106

Wilson Quevedo − *Helmholtz-Zentrum Berlin für Materialien und Energie, D-14109 Berlin, Germany*

Florian Trinter − *Molecular Physics, Fritz-Haber-Institut der Max-Planck-Gesellschaft, D-14195 Berlin, Germany; Institut für Kernphysik, Goethe-Universität Frankfurt, D-60438 Frankfurt am Main, Germany*; orcid.org/0000-0002-0891-9180

Bernd Winter − *Molecular Physics, Fritz-Haber-Institut der Max-Planck-Gesellschaft, D-14195 Berlin, Germany*; orcid.org/0000-0002-5597-8888

Complete contact information is available at: https://pubs.acs.org/10.1021/acs.jpcb.1c08172

Notes

The authors declare no competing financial interest.

https://doi.org/10.1021/acs.jpcb.1c08172
J. Phys. Chem. B 2022, 126, 229−238

■ ACKNOWLEDGMENTS

P.J. is thankful for the support from the European Regional Development Fund (project ChemBioDrug no. CZ.02.1.01/0.0/0.0/16_019/0000729). K.B. acknowledges funding from the IMPRS for Many Particle Systems in Structured Environments. This work was supported by the Project SVV 260586 of Charles University. F.T. and B.W. acknowledge support from the MaxWater initiative of the Max-Planck-Gesellschaft. R.S. and W.Q. acknowledge support from the Deutsche Forschungsgemeinschaft (DFG, German Research Society) through an Emmy-Noether grant (SE 2253/3-1). We thank the Helmholtz-Zentrum Berlin für Materialien und Energie for the allocation of synchrotron radiation beamtime. All authors thank the people of the mechanical workshop at the Fritz-Haber Institute, Berlin, and the Development Center of the IOCB, Prague, for their support. This work was supported by The Ministry of Education, Youth and Sports from the Large Infrastructures for Research, Experimental Development and Innovations Project "IT4Innovations National Supercomputing Center − LM2015070".

■ REFERENCES

(1) Winter, B.; Faubel, M. Photoemission from Liquid Aqueous Solutions. *Chem. Rev.* **2006**, *106*, 1176−1211.
(2) Tang, Y.; Shen, H.; Sekiguchi, K.; Kurahashi, N.; Mizuno, T.; Suzuki, Y. I.; Suzuki, T. Direct measurement of vertical binding energy of a hydrated electron. *Phys. Chem. Chem. Phys.* **2010**, *12*, 3653−3655.
(3) Elkins, M. H.; Williams, H. L.; Shreve, A. T.; Neumark, D. M. Relaxation Mechanism of the Hydrated Electron. *Science* **2013**, *342*, 1496−1499.
(4) Seidel, R.; Winter, B.; Bradforth, S. E. Valence Electronic Structure of Aqueous Solutions: Insights from Photoelectron Spectroscopy. *Annu. Rev. Phys. Chem.* **2016**, *67*, 283−305.
(5) Wieland, M.; Wilhein, T.; Faubel, M.; Ellert, C.; Schmidt, M.; Sublemontier, O. EUV and fast ion emission from cryogenic liquid jet target laser-generated plasma. *Appl. Phys. B: Lasers Opt.* **2001**, *72*, 591−597.
(6) Longetti, L.; Randulová, M.; Ojeda, J.; Mewes, L.; Miseikis, L.; Grilj, J.; Sanchez-Gonzalez, A.; Witting, T.; Siegel, T.; Diveki, Z.; et al. Photoemission from non-polar aromatic molecules in the gas and liquid phase. *Phys. Chem. Chem. Phys.* **2020**, *22*, 3965−3974.
(7) Buttersack, T.; Mason, P. E.; Jungwirth, P.; Schewe, H. C.; Winter, B.; Seidel, R.; McMullen, R. S.; Bradforth, S. E. Deeply cooled and temperature controlled microjets: Liquid ammonia solutions released into vacuum for analysis by photoelectron spectroscopy. *Rev. Sci. Instrum.* **2020**, *91*, 043101.
(8) Buttersack, T.; Mason, P. E.; McMullen, R. S.; Schewe, H. C.; Martinek, T.; Brezina, K.; Crhan, M.; Gomez, A.; Hein, D.; Wartner, G.; et al. Photoelectron spectra of alkali metal−ammonia microjets: From blue electrolyte to bronze metal. *Science* **2020**, *368*, 1086−1091.
(9) Åsbrink, L.; Lindholm, E.; Edqvist, O. Jahn-Teller effect in the vibrational structure of the photoelectron spectrum of benzene. *Chem. Phys. Lett.* **1970**, *5*, 609−612.
(10) Streets, D. G.; Potts, A. W. Photoelectron spectra of inner valence shells. Part 2.—Unsaturated hydrocarbons. *J. Chem. Soc., Faraday Trans. 2* **1974**, *70*, 1505−1515.
(11) Gelius, U. Recent progress in ESCA studies of gases. *J. Electron Spectrosc. Relat. Phenom.* **1974**, *5*, 985−1057.
(12) Baltzer, P.; Karlsson, L.; Wannberg, B.; Öhrwall, G.; Holland, D. M.; MacDonald, M. A.; Hayes, M. A.; Von Niessen, W. An experimental and theoretical study of the valence shell photoelectron spectrum of the benzene molecule. *Chem. Phys.* **1997**, *224*, 95−119.
(13) von Niessen, W.; Cederbaum, L. S.; Kraemer, W. P. The electronic structure of molecules by a many-body approach. I. Ionization potentials and one-electron properties of benzene. *J. Chem. Phys.* **1976**, *65*, 1378.
(14) Cederbaum, L. S.; Domcke, W.; Schirmer, J.; von Niessen, W.; Diercksen, G. H. F.; Kraemer, W. P. Correlation effects in the ionization of hydrocarbons. *J. Chem. Phys.* **1978**, *69*, 1591.
(15) Hirao, K.; Kato, H. Cluster expansion of the wavefunction. Ionization potentilals of benzene. *Chem. Phys. Lett.* **1983**, *98*, 340−344.
(16) Brezina, K.; Kostal, V.; Jungwirth, P.; Marsalek, O. Electronic Structure of the Solvated Benzene Radical Anion. *J. Chem. Phys.* **2021**, in press; DOI: 10.1063/5.0076115.
(17) Buttersack, T.; Mason, P. E.; McMullen, R. S.; Martinek, T.; Brezina, K.; Hein, D.; Ali, H.; Kolbeck, C.; Schewe, C.; Malerz, S.; et al. Valence and Core-Level X-ray Photoelectron Spectroscopy of a Liquid Ammonia Microjet. *J. Am. Chem. Soc.* **2019**, *141*, 1838−1841.
(18) Pohl, M. N.; Muchová, E.; Seidel, R.; Ali, H.; Sršeň, Š.; Wilkinson, I.; Winter, B.; Slavíček, P. Do water's electrons care about electrolytes? *Chemical Science* **2019**, *10*, 848−865.
(19) Credidio, B.; Pugini, M.; Malerz, S.; Trinter, F.; Hergenhahn, U.; Wilkinson, I.; Thürmer, S.; Winter, B. Quantitative electronic structure and work-function changes of liquid water induced by solute. *Phys. Chem. Chem. Phys.* **2021**, DOI: 10.1039/D1CP03165A.
(20) Winter, B.; Weber, R.; Hertel, I. V.; Faubel, M.; Jungwirth, P.; Brown, E. C.; Bradforth, S. E. Electron Binding Energies of Aqueous Alkali and Halide Ions: EUV Photoelectron Spectroscopy of Liquid Solutions and Combined Ab Initio and Molecular Dynamics Calculations. *J. Am. Chem. Soc.* **2005**, *127*, 7203−7214.
(21) Thürmer, S.; Malerz, S.; Trinter, F.; Hergenhahn, U.; Lee, C.; Neumark, D. M.; Meijer, G.; Winter, B.; Wilkinson, I. Accurate vertical ionization energy and work function determinations of liquid water and aqueous solutions. *Chemical Science* **2021**, *12*, 10558−10582.
(22) Perez Ramirez, L.; Boucly, A.; Saudrais, F.; Bournel, F.; Gallet, J.-J.; Maisonhaute, E.; Milosavljevic, A. R.; Nicolas, C.; Rochet, F. The Fermi level as an energy reference in liquid jet X-ray photoelectron spectroscopy studies of aqueous solutions. *Phys. Chem. Chem. Phys.* **2021**, *23*, 16224−16233.
(23) Seidel, R.; Pohl, M. N.; Ali, H.; Winter, B.; Aziz, E. F. Advances in liquid phase soft-x-ray photoemission spectroscopy: A new experimental setup at BESSY II. *Rev. Sci. Instrum.* **2017**, *88*, 073107.
(24) Follath, R.; Schmidt, J. S.; Siewert, F.; Holldack, K.; Zeschke, T.; Frentrup, W.; Schmitz, D.; Sawhney, K. J. S. Commissioning of the U49/2-PGM1 beamline. *AIP Conf. Proc.* **2003**, *705*, 348.
(25) King, G. C.; Tronc, M.; Read, F. H.; Bradford, R. C. An investigation of the structure near the L2,3 edges of argon, the M4,5 edges of krypton and the N4,5 edges of xenon, using electron impact with high resolution. *J. Phys. B: At. Mol. Phys.* **1977**, *10*, 2479.
(26) Kurahashi, N.; Karashima, S.; Tang, Y.; Horio, T.; Abulimiti, B.; Suzuki, Y. I.; Ogi, Y.; Oura, M.; Suzuki, T. Photoelectron spectroscopy of aqueous solutions: Streaming potentials of NaX (X = Cl, Br, and I) solutions and electron binding energies of liquid water and X-. *J. Chem. Phys.* **2014**, *140*, 174506.
(27) Malerz, S.; Trinter, F.; Hergenhahn, U.; Ghrist, A.; Ali, H.; Nicolas, C.; Saak, C.-M.; Richter, C.; Hartweg, S.; Nahon, L.; et al. Low-energy constraints on photoelectron spectra measured from liquid water and aqueous solutions. *Phys. Chem. Chem. Phys.* **2021**, *23*, 8246−8260.
(28) Tissot, H.; Gallet, J.-J.; Bournel, F.; Olivieri, G.; Silly, M. G.; Sirotti, F.; Boucly, A.; Rochet, F. The Electronic Structure of Saturated NaCl and NaI Solutions in Contact with a Gold Substrate. *Top. Catal.* **2016**, *59*, 605−620.
(29) Lundholm, M.; Siegbahn, H.; Holmberg, S.; Arbman, M. Core electron spectroscopy of water solutions. *J. Electron Spectrosc. Relat. Phenom.* **1986**, *40*, 163−180.
(30) Born, M. Volumen und Hydratationswärme der Ionen. *Eur. Phys. J. A* **1920**, *1*, 45−48.
(31) Donald, J.; Burgess, R. Thermochemical Data. In *NIST Chemistry WebBook*; NIST Standard Reference Database Number 69; National Institute of Standards and Technology, 2018.
(32) Kühne, T. D.; Iannuzzi, M.; Del Ben, M.; Rybkin, V. V.; Seewald, P.; Stein, F.; Laino, T.; Khaliullin, R. Z.; Schütt, O.;

Schiffmann, F.; “, CP2K; et al. An electronic structure and molecular dynamics software package -Quickstep: Efficient and accurate electronic structure calculations. *J. Chem. Phys.* **2020**, *152*, 194103.
(33) Perdew, J. P.; Burke, K.; Ernzerhof, M. Generalized Gradient Approximation Made Simple. *Phys. Rev. Lett.* **1996**, *77*, 3865.
(34) Zhang, Y.; Yang, W. Comment on “Generalized Gradient Approximation Made Simple. *Phys. Rev. Lett.* **1998**, *80*, 890.
(35) Adamo, C.; Barone, V. Toward reliable density functional methods without adjustable parameters: The PBE0 model. *J. Chem. Phys.* **1999**, *110*, 6158.
(36) Goerigk, L.; Grimme, S. A thorough benchmark of density functional methods for general main group thermochemistry, kinetics, and noncovalent interactions. *Phys. Chem. Chem. Phys.* **2011**, *13*, 6670−6688.
(37) Goedecker, S.; Teter, M.; Hutter, J. Separable dual-space Gaussian pseudopotentials. *Phys. Rev. B: Condens. Matter Mater. Phys.* **1996**, *54*, 1703.
(38) VandeVondele, J.; Hutter, J. Gaussian basis sets for accurate calculations on molecular systems in gas and condensed phases. *J. Chem. Phys.* **2007**, *127*, 114105.
(39) Guidon, M.; Hutter, J.; Vandevondele, J. Auxiliary Density Matrix Methods for Hartree−Fock Exchange Calculations. *J. Chem. Theory Comput.* **2010**, *6*, 2348−2364.
(40) Bussi, G.; Donadio, D.; Parrinello, M. Canonical sampling through velocity rescaling. *J. Chem. Phys.* **2007**, *126*, 014101.
(41) Hüser, F.; Olsen, T.; Thygesen, K. S. Quasiparticle GW calculations for solids, molecules, and two-dimensional materials. *Phys. Rev. B: Condens. Matter Mater. Phys.* **2013**, *87*, 235132.
(42) Wilhelm, J.; Ben, M. D.; Hutter, J. GW in the Gaussian and Plane Waves Scheme with Application to Linear Acenes. *J. Chem. Theory Comput.* **2016**, *12*, 3623−3635.
(43) Brezina, K.; Jungwirth, P.; Marsalek, O. Benzene Radical Anion in the Context of the Birch Reduction: When Solvation Is the Key. *J. Phys. Chem. Lett.* **2020**, *11*, 6032−6038.
(44) Edvardsson, D.; Baltzer, P.; Karlsson, L.; Wannberg, B.; Holland, D. M. P.; Shaw, D. A.; Rennie, E. E. A photoabsorption, photodissociation and photoelectron spectroscopy study of NH_3 and ND_3. *J. Phys. B: At., Mol. Opt. Phys.* **1999**, *32*, 2583.
(45) Tomas Martinek (Institute of Organic Chemistry and Biochemistry of the Czech Academy of Sciences, Flemingovo nám. 2, 166 10 Prague 6, Czech Republic), Ondrej Marsalek (Charles University, Faculty of Mathematics and Physics, Ke Karlovu 3, 121 16 Prague 2, Czech Republic), personal communication, August 2021.
(46) Duignan, T. T.; Baer, M. D.; Schenter, G. K.; Mundy, C. J. Electrostatic solvation free energies of charged hard spheres using molecular dynamics with density functional theory interactions. *J. Chem. Phys.* **2017**, *147*, 161716.
(47) Kathmann, S. M.; Kuo, I. F. W.; Mundy, C. J. Electronic Effects on the Surface Potential at the Vapor-Liquid Interface of Water. *J. Am. Chem. Soc.* **2008**, *130*, 16556−16561.
(48) Winter, B.; Weber, R.; Schmidt, P. M.; Hertel, I. V.; Faubel, M.; Vrbka, L.; Jungwirth, P. Molecular Structure of Surface-Active Salt Solutions: Photoelectron Spectroscopy and Molecular Dynamics Simulations of Aqueous Tetrabutylammonium Iodide. *J. Phys. Chem. B* **2004**, *108*, 14558−14564.
(49) Falkowska, M.; Bowron, D. T.; Manyar, H. G.; Hardacre, C.; Youngs, T. G. A. Neutron Scattering of Aromatic and Aliphatic Liquids. *ChemPhysChem* **2016**, *17*, 2043−2055.
(50) Hunt, P.; Sprik, M.; Vuilleumier, R. Thermal versus electronic broadening in the density of states of liquid water. *Chem. Phys. Lett.* **2003**, *376*, 68−74.
(51) Rumble, J. R., Ed. *CRC Handbook of Chemistry and Physics*, 101st ed.; CRC Press Taylor & Francis: Boca Raton, FL, 2020.

https://doi.org/10.1021/acs.jpcb.1c08172
J. Phys. Chem. B 2022, 126, 229−238